hydrogen

MDPI

Article

A Simple Study of Hydrogen Production from Recycled Aluminum Microparticles in Alkaline Media

Sergio Martínez-Vargas, José-Enrique Flores-Chan, Humberto-Julián Mandujano-Ramírez, Salatiel Pérez-Montejo, Damián Calan-Canche and Cristobal Patino-Carachure *

Facultad de Ingeniería, Universidad Autonoma del Carmen, Campus III, Ciudad del Carmen 24115, CP, Mexico; smartinez@pampano.unacar.mx (S.M.-V.); jeflores@pampano.unacar.mx (J.-E.F.-C.); hmandujano@pampano.unacar.mx (H.-J.M.-R.); sperez@pampano.unacar.mx (S.P.-M.); jodcalan@gmail.com (D.C.-C.)

* Correspondence: cpatino@pampano.unacar.mx; Tel.: +52-938-38-11018 (ext. 1702)

Abstract

Hydrogen (H_2) was produced from recycled aluminum microparticles (180–250, 300–425, and 425–500 μm) via alkaline hydrolysis using a 1.0 M NaOH solution to enhance oxide layer removal and aluminum dissolution. Maximum hydrogen flow rates of approximately 13, 15, and 19 mL·min^{-1} were obtained, confirming that smaller particle sizes promote faster reaction rates due to increased specific surface area. The hydrogen evolution exhibited two-stage kinetic behavior: an initial stage characterized by rapid aluminum dissolution and increasing H_2 production, followed by a gradual decline associated with the formation of a passivating $Al(OH)_3$ layer. Despite the higher reaction rates observed for smaller particles, the maximum cumulative hydrogen production was obtained for the intermediate particle size (363 μm, 132 mL), compared to 106 mL and 102 mL for 215 μm and 463 μm, respectively, indicating a trade-off between surface area and passivation effects. Kinetic analysis based on the shrinking core model showed excellent agreement (R^2 = 99.94–99.97%), with rate constants of 0.137, 0.064, and 0.050 min^{-1}. The relationship $k \propto d^{-n}$ ($n \approx 1.4$) suggests a mixed kinetic regime involving both surface reaction and diffusion through the $Al(OH)_3$ layer. These findings indicate that hydrogen generation can be modulated by particle size; however, the relatively low flow rates and yields limit its immediate practical applicability.

Keywords: recycled aluminum; hydrogen technology; gas flow evolution; alkaline medium

Check for updates

Academic Editors: Chiara Milanese and Rocio Maceíras Castro

Received: 14 February 2026
Revised: 17 April 2026
Accepted: 18 April 2026
Published: 22 April 2026

Copyright: © 2026 by the authors. Licensee MDPI, Basel, Switzerland. This article is an open access article distributed under the terms and conditions of the Creative Commons Attribution (CC BY) license.

1. Introduction

In recent years, clean energy sources have gained increasing global attention, with hydrogen emerging as a promising alternative to reduce dependence on fossil fuels. Currently, global hydrogen production is dominated by natural gas steam reforming, followed by other hydrocarbons (~30%), coal gasification (~18%), water electrolysis (~3.9%), and minor alternative routes (~0.1%) [1–7]. However, these conventional processes are associated with significant greenhouse gas emissions, highlighting the need for more sustainable production pathways [8,9].

In addition to production, hydrogen storage remains a major challenge, particularly for portable and on-demand energy systems. Conventional storage methods, such as compressed gas and metal hydrides, present limitations related to efficiency, cost, and energy consumption. Although materials such as lithium borohydride ($LiBH_4$) offer high energy density, their practical application is constrained by cost and scalability issues [10–13].

A promising alternative for hydrogen generation is the reaction between metallic aluminum (Al) and water. Aluminum is an attractive energy carrier due to its abundance, recyclability, and high theoretical hydrogen yield (~1.245 L g^{-1} at standard temperature and pressure) [14–17]. The use of aluminum waste, such as beverage cans, provides an additional advantage by enabling a sustainable and circular approach to hydrogen production, which has recently gained increasing attention in waste-to-energy strategies [18–20]. However, aluminum hydrolysis is hindered by the presence of a passivating Al_2O_3 layer (2–5 nm), which limits its reactivity [21]. To overcome this limitation, several activation strategies have been proposed, including acidic or alkaline media and mechanical treatments [22]. Among these, alkaline activation is particularly attractive due to its simplicity, low cost, and rapid reaction kinetics. The main reactions of aluminum with NaOH in aqueous solution are described by Equations (1)–(3), where NaOH acts as a promoter and is regenerated during the process [23–27]:

$$2Al(s) + 6H_2O(l) + 2NaOH(s) \rightarrow 2NaAl(OH)_4(aq) + 3H_2(g) \quad (1)$$

$$2NaAl(OH)_4(aq) \rightarrow 2NaOH(s) + 2Al(OH)_3(aq) \quad (2)$$

$$2Al(s) + 6H_2O(l) \rightarrow 2Al(OH)_3(aq) + 3H_2(g) \quad (3)$$

NaOH consumed in (1) is regenerated in (2), completing the overall process in (3). However, passivation by $Al(OH)_3$ and Al_2O_3 films can reduce hydrolysis by ~30%, lowering H_2 yield by ~33% [28].

Nevertheless, the formation of $Al(OH)_3$ introduces diffusional limitations, reducing hydrogen yield and reaction rate [25]. Recent studies have highlighted that hydrogen generation from aluminum in alkaline media is frequently governed by diffusion through the product layer or by mixed kinetic regimes, depending on particle size and reaction conditions [18,29].

Although hydrogen production from aluminum has been widely studied, most kinetic analyses have focused on high-purity aluminum under controlled conditions, limiting their applicability to real systems. In contrast, recycled aluminum exhibits heterogeneity in particle size, morphology, and surface composition, which significantly affects reaction kinetics [30].

In this work, a kinetic–empirical approach is applied to hydrogen generation from recycled aluminum microparticles in alkaline media, with particular emphasis on particle size effects. The study identifies an optimal particle size that maximizes cumulative hydrogen production, while smaller particles enhance reaction rates. Additionally, kinetic parameters based on the shrinking core model (SCM) [31], together with regression-based correlations, are established to describe the dependence of hydrogen generation on particle size. The results further support the presence of a mixed kinetic regime involving both surface reaction and diffusion through the $Al(OH)_3$ layer.

These findings provide a realistic framework for aluminum–water reactions and support the design of sustainable hydrogen generation systems from recycled materials. The obtained kinetic parameters enable preliminary small-scale reactor design; however, extrapolation to significantly different particle sizes requires experimental validation, as it may modify the controlling mechanisms described by the SCM.

2. Materials and Methods

Aluminum beverage cans were used to obtain aluminum alloy ingot. The chemical components of each can part were as follows: AA 5182/H48 (beverage can lids) [32], AA 5042/H18 (beverage can tabs) [33], and AA 3104/H19 (beverage can body) [34], as shown in Table 1.

Table 1. Chemical composition of the can's alloys [14,19,20,28,32–34].

Alloy		Composition %					
		Si	Fe	Cu	Mn	Mg	Cr
AA 5182/H48	Min	0.00	0.00	0.00	0.20	4.00	0.00
(Beverage can lids)	Max	0.20	0.35	0.15	0.50	5.00	0.00
AA 5042/H18	Min	0.00	0.00	0.00	0.20	3.00	0.00
(Beverage can tabs)	Max	0.20	0.35	0.15	0.50	4.00	0.10
AA 3104/H19	Min	0.00	0.00	0.05	0.80	0.80	0.00
(Beverage can body)	Max	0.20	0.80	0.25	1.40	1.30	0.05

First, the paint covering the cans was removed using sandpaper and solvent. Subsequently, the cans were compacted. Figure 1a illustrates the main steps involved in the recycling of aluminum cans. (1) Preparation: Aluminum beverage cans were collected and mechanically shredded to reduce their volume prior to melting. (2) Melting and casting: The shredded cans were placed in a crucible inside a melting furnace and heated to approximately 700 °C (1292 °F). Once completely molten, the aluminum was poured into a mold and allowed to cool at room temperature to form an ingot. (3) Mechanical filing: The obtained aluminum ingot was mechanically filed using a 25 cm (10-inch) Bellota steel flat file (model 6400110F1BL) in order to produce recycled aluminum powder. (4) Magnetic separation: A permanent neodymium magnet was passed repeatedly over the aluminum powder to remove any ferrous contaminants. (5) Particle size classification: The iron-free aluminum powder was sieved to classify the particle size using standard sieves in accordance with ASTM E11-22 [35].

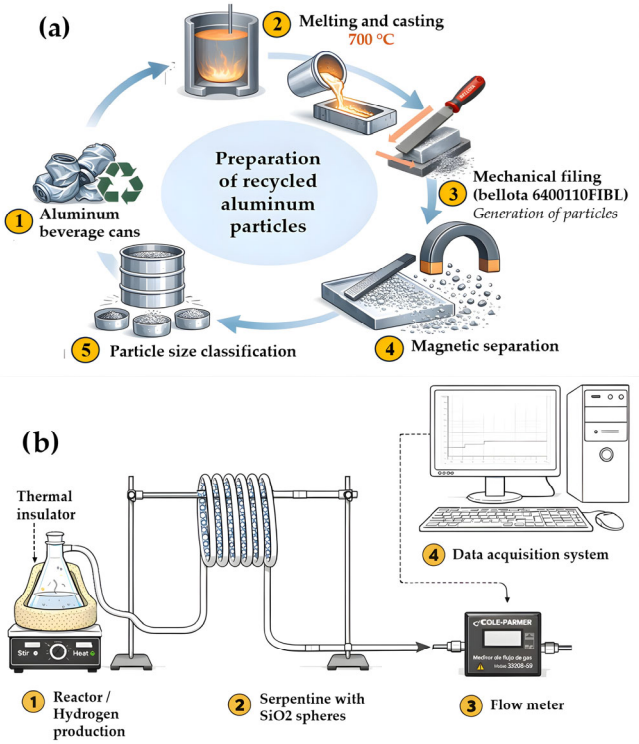


Figure 1. Schematic representations for (**a**) obtaining recycled aluminum powders and (**b**) quantification of hydrogen production [36] from recycled aluminum using NaOH.

It is worth mentioning that Jayaraman et al. [17] reported that the specific surface area and reaction temperature influence the reaction rate of aluminum with water, which in turn

modifies the yield of hydrogen generation and the compounds formed. For this reason, particles of different sizes were obtained by gradually filing.

Next, numbered sieves ranging from 230 to 35 (ASTM E11-22) were used to classify the particles. The resulting particle size distribution is presented in the histogram shown in Figure 2. Based on this distribution, three particle size ranges were selected for testing: 180–250 μm, 300–425 μm, and 425–500 μm, as indicated by the arrows in Figure 2.

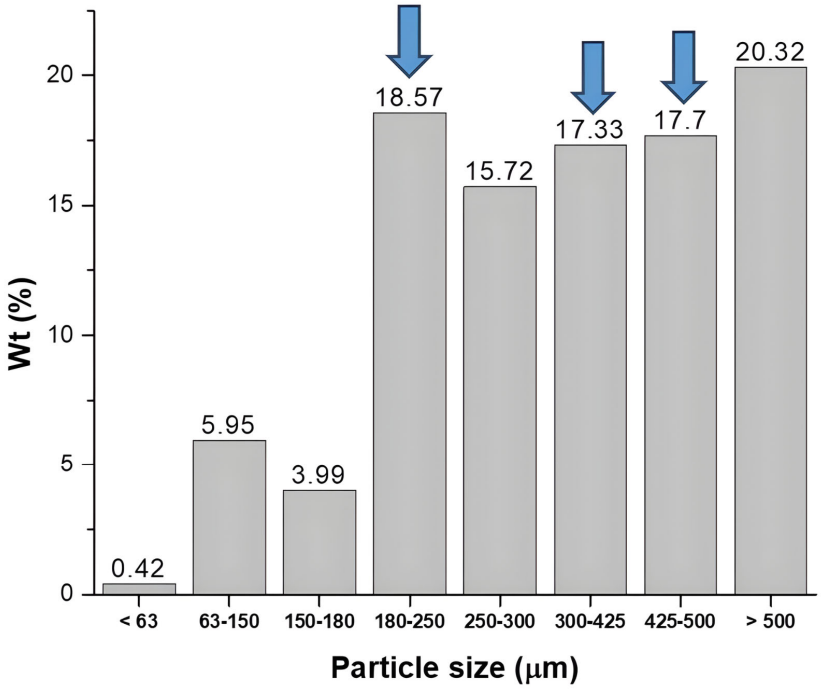


Figure 2. Particle size distribution of sieved aluminum powders (mesh 230–35), highlighting the selected size ranges (180–250, 300–425, and 425–500 μm).

Figure 1b shows a schematic of the custom-made laboratory equipment for quantification of the hydrogen production rates and its performance from recycled aluminum in alkaline medium. To guarantee the reliability and reproducibility of the kinetic measurements, rigorous control of the experimental boundary conditions was implemented. The reaction was carried out in a 250 mL Kitasato flask operating at local atmospheric pressure. To eliminate external mass transfer resistance and ensure homogeneous contact between the aluminum particles and the 1.0 M NaOH solution, constant magnetic stirring at 400 rpm was applied using a hot plate stirrer. The reaction temperature was strictly maintained at 55 ± 1 °C using a PID controller integrated into the heating plate, complemented by an external thermal insulator to mitigate heat loss from the exothermic reaction.

Prior to each experimental run, the entire setup—including the reactor, the silica gel (SiO_2) serpentine, and the connecting hoses—was subjected to a leak test by temporarily pressurizing the system and monitoring for pressure drops, thereby ensuring complete hermeticity. The volumetric hydrogen flow rate was continuously recorded using a Cole-Parmer digital flowmeter. To validate the measurements, the flowmeter was pre-calibrated using a standard water displacement method. The overall experimental uncertainty for the volumetric flow measurements, considering the instrumental sensitivity (±0.01 mL/min) and propagated errors, was estimated to be less than 5%. Given that the theoretical maximum hydrogen yield matched the integrated volume obtained, the purity of the evolved gas was considered highly consistent with the expected reaction stoichiometry (Equations (1) and (3)), with the silica gel effectively preventing moisture interference.

Three repetitions were performed for each particle size distribution. The same procedure was carried out for particles sized 300–425 μm and 425–500 μm. Hydrogen production occurred through Al–NaOH reactions (see Equations (4) and (5)), in a cyclic process where environmental pollution is avoided and aluminum is efficiently reused [14,15,18–20].

$$2Al(s) + 2NaOH(s) + 6H_2O(l) \rightarrow 2Al(OH)_3(aq) + 3H_2(g) \quad (4)$$

$$2Al(s) + 2Al(OH)_3(aq) + 4NaOH(s) + 6H_2O(l) \rightarrow 4NaAl(OH)_4(aq) + 3H_2(g) \quad (5)$$

Bayerite, a form of aluminum hydroxide ($Al(OH)_3$), dissolves in NaOH to produce soluble $NaAl(OH)_4$. This reaction is a key step in the Bayer process [37]. The ratio of the $Al(OH)_3(aq)$ (Bayerite) to $NaAl(OH)_4(aq)$ on the reaction (5) is basically independent of temperature [38]. Moreover, the oxidative behavior of aluminum in hydrogen production strongly depends on the nature of the dissolved species present when it interacts with aqueous solutions. Machanás et al. have taken advantage of this behavior to develop a new sustainable method (the AlHidrox process) to produce hydrogen from water under mild conditions, in such a way that they have achieved to reduce the surface passivation of aluminum for produce hydrogen through a process that allows reduced hydrogen production costs [39].

In early moments aluminum comes into contact with the environment, it forms on the aluminum an oxide film (Al_2O_3) of about 2–4 nanometers on its surface [40]. This Al_2O_3 on the aluminum surface is not homogeneous and has imperfections, through its ambient humidity comes into contact with aluminum, forming aluminum hydroxide $Al(OH)_3$ on its surface and releasing H_2 into the environment (see Equation (3)). The formation and consequent growth of $Al(OH)_3$ on the aluminum surface minimizes the reaction with water molecules in the early moments. Although in alkaline conditions Equation (1), is favored by the destruction of Al_2O_3 on the surface, giving reaction product $NaAl(OH)_4$ and the release of hydrogen into the environment. Hydrogen generation is increased by the interaction of the alkaline medium (NaOH) with the aluminum surface and by the same hydrogen generated by the embrittlement mechanism [41].

In addition, the average flow and the average volume of hydrogen produced were determined where different stages during hydrogen production were identified. The compounds and phases formed from the residual products were characterized by X-ray diffraction (XRD), and scanning electron microscopy (SEM).

To establish a rigorous kinetic framework beyond empirical correlations, the cumulative volume of hydrogen generated in the reactor was converted into the aluminum conversion degree (α), defined as: $\alpha = \frac{V_t}{V_{max}}$, where V_t is the hydrogen volume at time t and V_{max} is the total hydrogen volume produced.

The experimental conversion–time profiles were analyzed using the Shrinking Core Model [42]. To identify the rate-controlling step of the solid–liquid reaction between aluminum and the NaOH solution, the data were fitted to the following fundamental expressions:

$$\text{Surface chemical reaction control: } 1 - (1 - \alpha)^{1/3} = k_r t.$$

$$\text{Diffusion control through the product layer: } 1 - 3(1 - \alpha)^{2/3} + 2(1 - \alpha) = k_d t.$$

where k_r and k_d are the apparent rate constants for chemical reaction and diffusion control, respectively.

Finally, the reaction rates were normalized with respect to the initial surface area, calculated under the assumption of spherical particle morphology and mean diame-

ters for the three sieved size fractions, in order to decouple intrinsic kinetic effects from geometric influences.

3. Results

Figure 3 shows the three hydrogen production flux curves as a function of time for each particle size distributions ((a) 425–500 μm, (b) 300–425 μm, and (c) 180–250 μm). The behavior of the H_2 fluxes for the three particle sizes is described in two stages (separated by a dashed line): the first occurs in the initial moments of interaction of the aluminum particles with the NaOH solution, which tends to increase to a maximum flow rate (Q_{max}) of approximately 13 mL/min. Then, in the second stage, the flow rates tend to decrease to values close to zero. This effect is due to the increased thickness of the Al_2O_3 coating on the aluminum particles according to the Cabrera–Mott mechanism [43]. On the other hand, an increase in hydrogen flux is observed as the particle size decreases; for example, in size distribution (b) the Q_{max} reached varies from 13 to 16 mL/min, while in distribution (c) it varies from 15 to 22 mL/min, from this it can be deduced that the decrease in particle size plays an important role in the kinetics of hydrogen production.

An inflection point can also be seen in the curve, after passing through the maximum indicated by arrows for each particle distribution. This suggests a second hydrogen production reaction, albeit at a lower rate compared to the first region.

Figure 4a presents the average hydrogen flow curve, where the behavior of each hydrogen production process can be observed in greater detail. Also, it shows that the Q_{max} obtained for each particle size distribution (a), (b) and (c) are 13.13, 14.68, and 18.77 mL/min, respectively, indicating an increase as particle size decreases. Furthermore, the curves indicate hydrogen production reaction times (t_r) of 29.30, 25.12, and 14.86 min for cases (a), (b), and (c), respectively, revealing a decrease in t_r with decreasing particle size.

Figure 4b shows the cumulative volume obtained from the H_2 production flow data as a function of time. This figure shows that particle size curve (a) accumulates a volume of 102 mL, while curve (b) accumulates 132 mL and curve (c) 106 mL of hydrogen. This interesting result suggests the following explanation: in the first region, the particles react very rapidly, achieving a very high flow rate and becoming coated with $Al(OH)_3$, which quickly decreases the hydrogen production reaction, resulting in a smaller cumulative volume. Thus, larger particles have a longer reaction time compared to smaller particles.

To quantitatively evaluate the effect of the average particle size (d_p) on the Q_{max} and t_r, a statistical analysis of the experimental results was carried out. Table 2 presents the descriptive statistics of the variables studied. The average particle size (dp = 215, 363 and 463 μm) was used as the input factor, while the Q_{max} and the t_r obtained in each experiment were considered as the response variables.

Table 2. Descriptive statistics of the maximum hydrogen flow rate (Q_{max}) and reaction time (t_r) for different average particle sizes.

Descriptive Statistics	d_p Average Particle Size (μm)		
	215	**363**	**463**
Qmax	22.41 18.40 15.51	15.05 15.77 13.23	12.81 13.17 13.44
$\overline{x} = \frac{\sum x_i}{n} \pm \frac{\sigma}{\sqrt{n}}$	18.77 ± 2.00	14.68 ± 0.76	13.14 ± 0.18
$s^2 = \frac{\sum (x_i - \overline{x})^2}{n-1}$	12.00	1.71	0.10

Table 2. *Cont.*

Descriptive Statistics	d_p Average Particle Size (µm)		
	215	**363**	**463**
$\sigma = \sqrt{s^2}$	3.47	1.31	0.32
t_r	14.55 14.85 15.18	24.36 24.26 26.75	32.56 27.85 27.48
$\overline{x} = \frac{\sum x_i}{n} \pm \frac{\sigma}{\sqrt{n}}$	14.86 ± 0.18	25.12 ± 0.81	29.30 ± 1.64
$s^2 = \frac{\sum (x_i - \overline{x})^2}{n-1}$	0.10	1.99	8.02
$\sigma = \sqrt{s^2}$	0.32	1.41	2.83

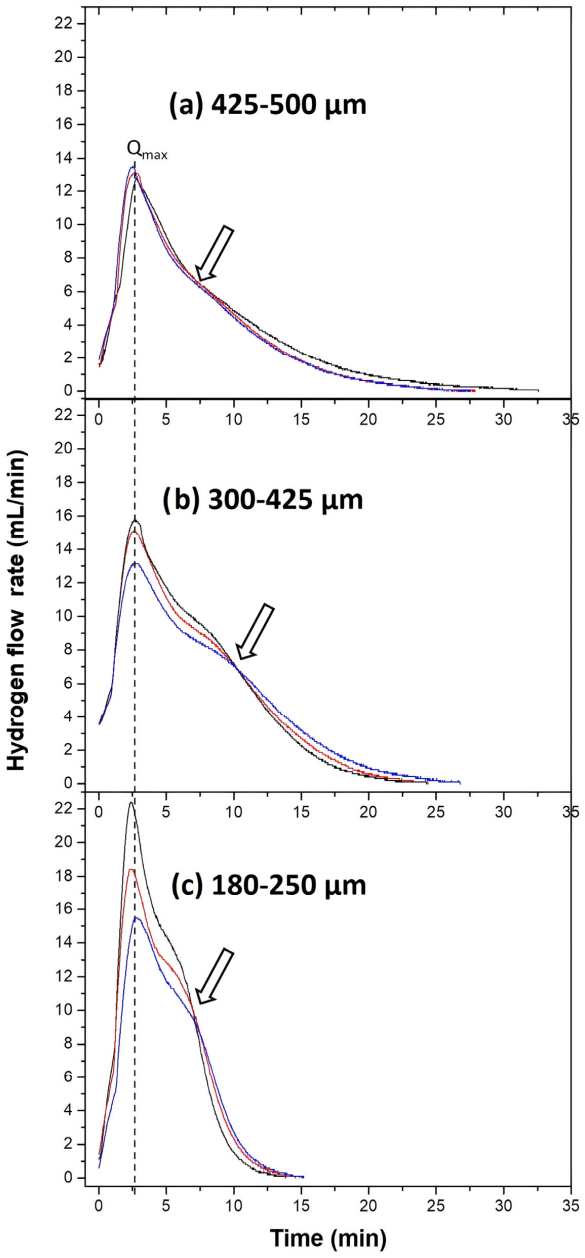


Figure 3. Hydrogen flow rate versus time for particle sizes of (**a**) 425–500 µm, (**b**) 300–425 µm, and (**c**) 180–250 µm.

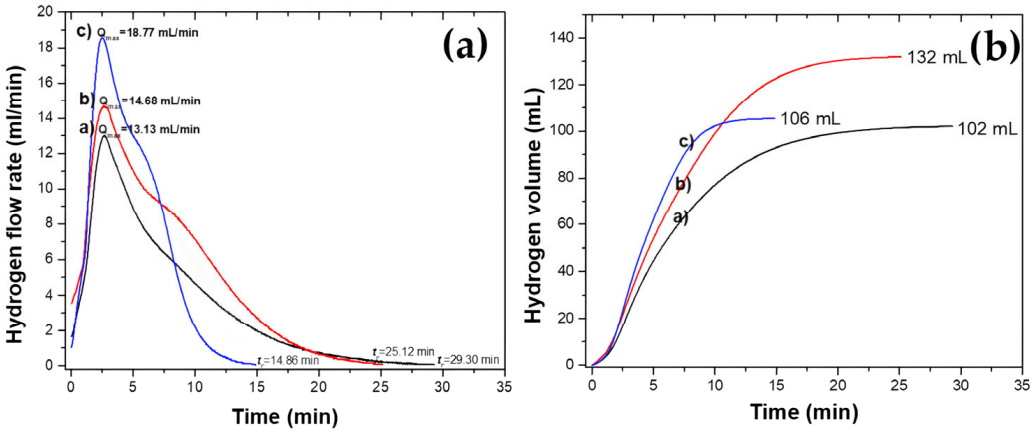


Figure 4. (**a**) Average hydrogen flow rate and (**b**) cumulative volume versus time for different particle sizes.

To characterize the dispersion of the experimental data, the main statistical parameters were calculated. All experiments were performed in triplicate (n = 3). The data are expressed as the mean ± the standard error of the mean (*SEM**), which was chosen to illustrate the precision of the estimated average values for the maximum hydrogen flow rate and reaction time across the different particle size distributions.

Based on the observed behavior of the average Q_{max} values as a function of particle size, a power-law model is proposed to describe the relationship between these variables, expressed as follows:

$$Q_{max} = a\, d_p^{-b} \tag{6}$$

where:

Q_{max} represents the dependent variable;
d_p corresponds to the independent variable;
a is a proportionality constant;
b is the characteristic exponent of the model.

To determine the constants a and b using linear regression techniques, a natural logarithmic transformation was applied to both sides of Equation (6). By taking the natural logarithm (ln), the following expression (Equation (7)) is obtained:

$$ln(Q_{max}) = ln(a) - b\, ln(d_p) \tag{7}$$

This transformation converts the power-law model into a linear relationship between the variables: $y = ln(Q_{max})$ and $x = ln(d_p)$ which allows the model parameters to be estimated using simple linear regression. Based on the average values of the maximum flow rate and particle size presented in Table 2, a data linearization procedure was performed, and the results are summarized in Table 3. Subsequently, Figure 5 shows the graphical representation of $ln(Q_{max})$ as a function of $ln(d_p)$. This plot allows the parameters of the power-law model to be determined from the slope and the intercept of the fitted linear regression line.

Table 3. Variable transformation used for the linearization of the power-law model.

$x = d_p$ (μm)	$y = Q_{max}$ (mL/min)	$ln(x)$	$ln(y)$
215	18.77 ± 2.00	5.37064	2.93226
363	14.68 ± 0.76	5.89440	2.68649
463	13.14 ± 0.18	6.13773	2.57566

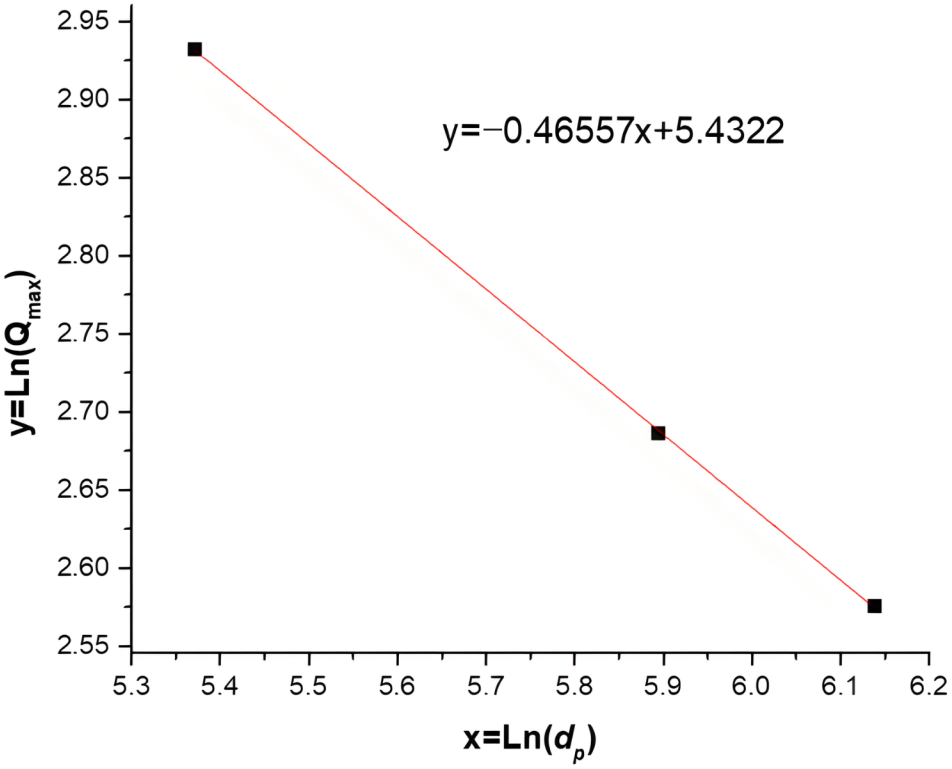


Figure 5. Determination of the constants a and b by linear regression of the power-law model.

Through linear regression fitting of the logarithmically transformed data, the parameters of the proposed power-law model were determined. In this linear representation, the slope of the fitted line corresponds to the value of −b, while the intercept represents the term $ln(a)$.

Based on this procedure, the following power-law model was obtained, which describes the relationship between particle size and the maximum hydrogen flow rate:

$$Q_{max} = 228.652\, d_p^{-0.46557} \quad (8)$$

The statistical analysis of the fit showed a coefficient of determination $R^2 \approx 0.9999$, indicating that approximately 99.99% of the observed variability in the maximum flow rate can be explained by the proposed power-law model (see Figure 6a).

On the other hand, in order to analyze the relationship between particle size (d_p) and reaction time (t_r), the average values reported in Table 2 were used. Based on a preliminary observation of the data behavior, a simple linear regression model was proposed, described by Equation (9):

$$t_r = m\, d_p + b \quad (9)$$

where:

d_p = particle size (μm);
t_r = reaction time (min);
m = slope of the linear regression;
b = y-intercept.

The parameters corresponding to the slope m and the intercept b were determined by linear regression fitting, and the results are presented in Figure 6b. From this analysis, the following empirical expression was obtained (Equation (10)):

$$t_r = 0.059\, d_p + 2.5998 \quad (10)$$

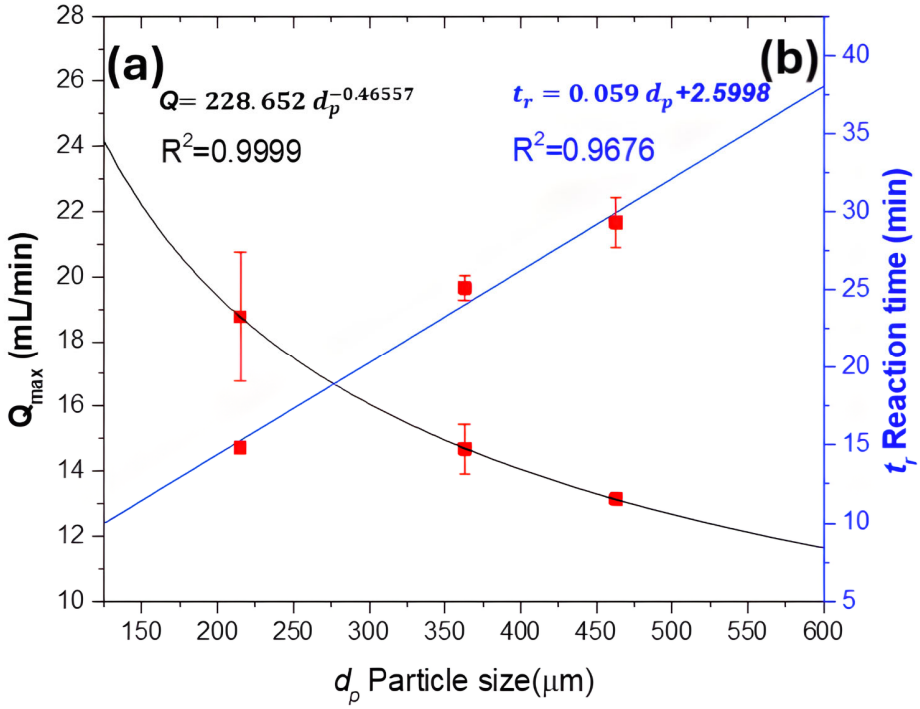


Figure 6. Relationship between particle size and the experimental response variables: (**a**) maximum hydrogen flow rate described by the power-law model and (**b**) reaction time described by the linear regression model. Error bars represent the standard error of the mean (*SEM**) based on n = 3 independent replicates.

To determine the microstructural features of the samples after the experiments, scanning electron microscopy (SEM) was performed, as shown in Figure 7. Backscattered electron imaging reveals a homogeneous powder distribution at a magnification of 2000× (Figure 7a). A gray-scale contrast associated with oxidized particles coated with $Al(OH)_3$ can also be observed. For a more detailed observation, secondary electron imaging was conducted at a magnification of 5000× (Figure 7b), where the acicular growth of the $Al(OH)_3$ phase on the surface of the aluminum alloy particles is clearly visible. Furthermore, the coexistence of the main alloying elements was identified by Energy-dispersive X-ray spectroscopy (EDS), as presented in Figure 7c. Oxygen is detected in the highest proportion, which is attributed to the oxidation of aluminum. The remaining elements, including Fe, Mg, Mn, Na, and Si, correspond to the alloy constituents listed in Table 1. Chlorine (Cl) was also detected, which is attributed to impurities in the NaOH reagent.

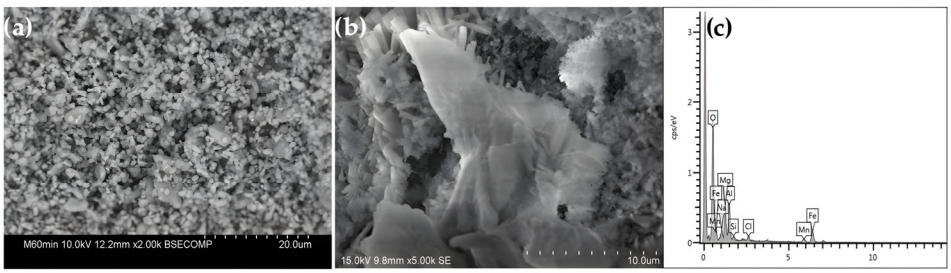


Figure 7. SEM images of aluminum particles after NaOH reaction: (**a**) $Al(OH)_3$-coated particles; (**b**) 5000× magnification showing acicular $Al(OH)_3$ growth; (**c**) EDS confirms alloying elements and oxidation.

These microstructural observations support the kinetic results obtained during hydrogen generation, indicating that the reaction proceeds through surface oxidation of

aluminum particles followed by the precipitation of $Al(OH)_3$, which progressively modifies the reactive surface during the process.

The samples were subjected before and after to X-ray diffraction (XRD) to determine the phases of the byproducts of the production reaction between aluminum and the alkaline medium of sodium hydroxide (see Figure 8). Figure 8a shows the XRD pattern of the powder sample before being subjected to the hydrogen production reaction. It displays the typical crystalline structure of aluminum with its respective principal crystallographic planes (111), (200), (220), and (311), which diffract in this 2θ region according to Bragg's law. It is important to note that the alloying chemical components shown in Table 1 are not visible in the pattern. This is because the alloying elements are randomly distributed within the aluminum structure and at grain boundaries, as previously reported [44]. According to the random distribution of alloying elements within the aluminum matrix and at grain boundaries, several critical microstructural effects occur. The XRD pattern corresponding to the sample subjected to the hydrogen production reaction is shown in Figure 8b, where it is possible to determine the coexistence of phases such as: Al, $Al(OH)_3$, and $NaAl(OH)_4$. These results confirm that hydrogen generation occurs through the alkaline oxidation of aluminum, leading to the formation of hydroxide and aluminate phases (Equations (1)–(5)), while residual metallic Al indicates that the reaction proceeds progressively from the particle surface.

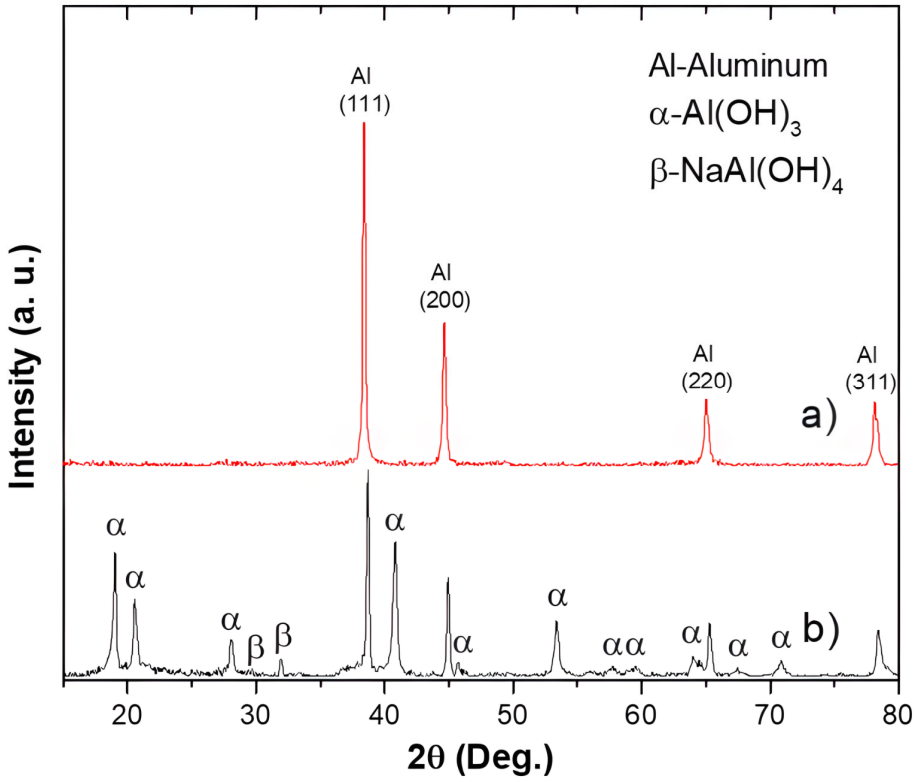


Figure 8. XRD patterns of aluminum powders before (**a**) and after (**b**) reaction with NaOH solution.

4. Discussion

The differences in hydrogen generation kinetics (Figure 3) are primarily attributed to particle size effects resulting from the mechanical fragmentation of the aluminum ingot. Particle size reduction increases specific surface area and surface energy, thereby enhancing aluminum dissolution in alkaline media [32,36,40]. In addition, smaller particles exhibit a higher density of surface defects, facilitating oxide disruption, and accelerating hydrogen evolution [22,45–48].

For the largest particles (425–500 μm), a lower Q_{max} (~13 mL·min^{-1}) and longer induction time (~30 min) were observed. In contrast, the intermediate fraction (300–425 μm) showed improved performance (~15 mL·min^{-1}) with more sustained hydrogen production, indicating particle size-dependent kinetics [49]. The smallest particles (180–250 μm) reached the highest Q_{max} (~19 mL·min^{-1}) rapidly, followed by a decline due to the formation of an $Al_2O_3/Al(OH)_3$ layer that limits mass transfer [50,51]. While smaller particles enhance initial reactivity, the intermediate size range provides a better balance between surface area and reaction stability, resulting in the highest cumulative hydrogen production (Figure 4b). Hydrogen generation from recycled aluminum is comparable to that of activated or high-purity systems, despite simple operating conditions, highlighting its practical advantages [25,52–56]. The observed behavior is consistent with literature reports, with differences attributed to particle morphology, oxide thickness, and impurities [25,57].

The power-law model indicates a strong correlation between particle diameter and maximum hydrogen flow rate. The exponent (b = 0.46557) suggests a nonlinear inverse relationship characteristic of surface-dependent and mass transfer-controlled processes. Linear regression analysis yielded R^2 = 0.9676, indicating that 96.76% of the variability in reaction time is explained by particle size. The positive slope (m = 0.059 min·μm^{-1}) confirms that reaction time increases with particle size, consistent with surface-controlled kinetics, which is consistent with the research cited above.

On the other hand, SEM micrographs and XRD patterns confirmed the precipitation and acicular growth of an $Al(OH)_3$ layer on the aluminum surface, a well-known feature of aluminum hydrolysis systems [58,59]. The progressive thickening of this layer acts as a diffusion barrier, hindering the transport of the alkaline solution toward the unreacted aluminum core [59]. Consequently, the reaction follows a shrinking unreacted core mechanism, consistent with the classical core–shell model [42].

To further elucidate the kinetic mechanism, experimental data were analyzed using the Shrinking Core Model. Initially, the exposed aluminum surface is in direct contact with the NaOH solution, resulting in a high hydrogen evolution rate (Figure 4b). As the reaction progresses, a porous product layer forms around the unreacted core, requiring diffusion of the reaction through this layer to sustain the reaction.

Assuming diffusion control through the product layer for spherical particles, the conversion-dependent expression (Equation (11)) was applied:

$$F_d(\alpha) = 1 - 3(1-\alpha)^{2/3} + 2(1-\alpha) = k_d t. \quad (11)$$

where $\alpha = V_t/V_{max}$ is the conversion degree, V_t is the cumulative hydrogen volume at time t, and V_{max} is the total hydrogen volume. It is important to note that 1 g of aluminum theoretically yields 1245 mL of hydrogen at standard temperature and pressure. In this work, the reported total volume corresponds to the cumulative hydrogen volume obtained experimentally under these conditions, as presented in Figure 4b. The parameter k_d (min^{-1}) represents the apparent diffusion rate constant.

The linear regions of the transformed data (Figure 9) allowed the determination of kd values of 0.137, 0.064, and 0.05 min^{-1} for increasing particle sizes, with high coefficients of determination ($R^2 > 0.99$), supporting diffusion through the product layer as the rate-controlling step [29,42].

The calculated rate constants decrease with increasing particle size, which is consistent with heterogeneous reaction theory [29]. This trend is attributed to the increased diffusion path length and mass transfer resistance imposed by the growing hydroxide layer [4,6]. Additionally, the effective diffusivity evolves during the reaction due to structural densification and porosity changes [20,58].

The kinetic constant follows a power-law dependence on particle size ($k \propto d^{-n}$). Linear regression of the logarithmic form yields $n \approx 1.4$, indicating a mixed kinetic regime between chemical reaction control (n = 1) and diffusion control (n = 2), in agreement with the Shrinking Core Model [30,42]. This supports a multi-step mechanism involving simultaneous interfacial reaction, diffusion, and mass transfer processes, as reported in recent studies of aluminum–water systems [23]. It should be noted that this relationship is valid only within the evaluated particle size range, as variations in morphology and passivation layer properties may alter the controlling mechanisms [22].

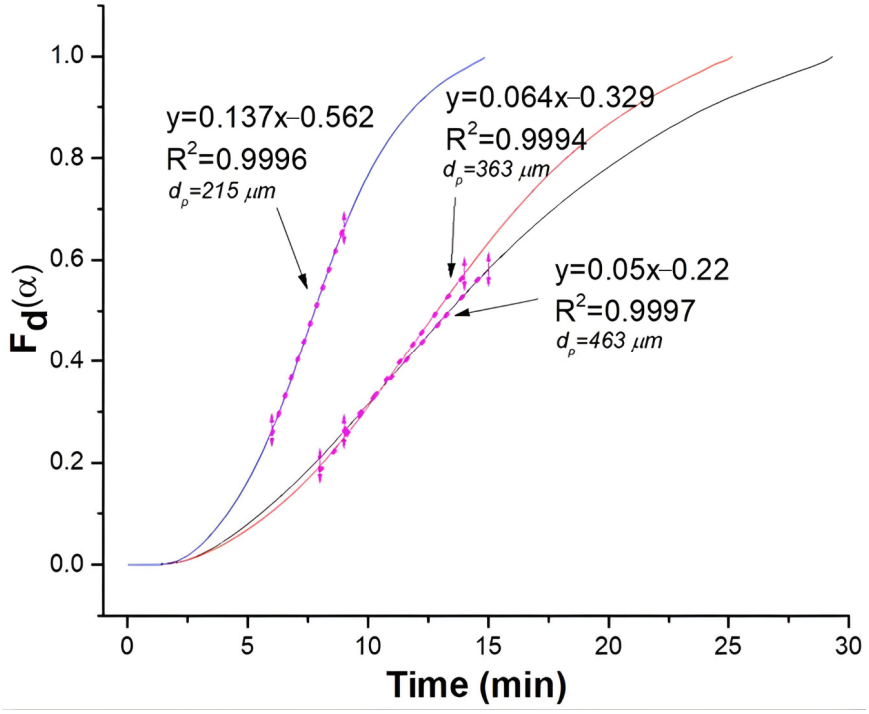


Figure 9. Linear fitting of the diffusion-controlled shrinking core model by plotting $F_d(\alpha)$ as a function of time for different aluminum particle sizes. The slopes of the fitted lines correspond to the apparent diffusion rate constants (k_d), showing excellent agreement with the model ($R^2 > 0.99$).

Overall, the progressive growth and densification of the oxide/hydroxide layer significantly increase intraparticle diffusion resistance of OH^- ions toward the unreacted core, explaining the gradual decline in hydrogen generation rate. This behavior is consistent with modified Shrinking Core Model approaches that account for variable diffusivity and structural evolution within the product layer [42,59].

Finally, the predictive capability of the regression models is restricted to the particle size range of 180 to 500 μm. Extrapolation beyond this interval may lead to significant deviations, as variations in particle size can alter the underlying kinetic mechanisms governing the process.

5. Conclusions

Hydrogen was successfully generated from recycled aluminum cans via alkaline hydrolysis using a 1.0 M NaOH solution, which effectively promotes oxide layer removal and aluminum dissolution.

The results show that hydrogen production rate increases as particle size decreases due to the higher specific surface area, with the smallest range (180–250 μm) exhibiting the highest reaction rate and shortest reaction time. In contrast, the maximum cumulative hydrogen production was obtained for the intermediate particle size (363 μm, 132 mL),

compared to 106 mL and 102 mL for 215 μm and 463 μm, respectively, indicating a trade-off between reaction rate and passivation effects.

The hydrogen evolution process followed a two-stage kinetic behavior: an initial stage dominated by rapid aluminum dissolution, followed by a slower stage associated with the formation of a passivating $Al(OH)_3$ layer.

The dependence of hydrogen generation on particle size was adequately described by both power-law and regression models, confirming that smaller particles enhance reaction kinetics, while larger particles extend reaction time.

The shrinking core model provided an excellent fit (R^2 = 99.94–99.97%), with rate constants of 0.137, 0.064, and 0.050 min^{-1}. The relationship $k \propto d^{-n}$ ($n \approx 1.4$) indicates a mixed kinetic regime, where surface reaction dominates at early stages, while diffusion through the $Al(OH)_3$ layer becomes increasingly significant over time.

SEM/XRD analyses confirmed the formation of $Al(OH)_3$, supporting the proposed mechanism. Despite the ability to control hydrogen generation through particle size, the relatively low flow rates and yields, together with the absence of purity and energy analyses, limit practical applicability. Therefore, these results should be considered as a laboratory-scale kinetic assessment.

Author Contributions: Conceptualization, C.P.-C. and S.M.-V.; methodology, S.P.-M.; validation, C.P.-C., S.M.-V. and J.-E.F.-C.; formal analysis, D.C.-C.; investigation, S.P.-M.; resources, D.C.-C.; data curation, H.-J.M.-R.; writing—original draft preparation, C.P.-C. and S.M.-V.; writing—review and editing, C.P.-C. and S.M.-V. All authors have read and agreed to the published version of the manuscript.

Funding: This research received no external funding.

Data Availability Statement: The original contributions presented in this study are included in the article. Further inquiries can be directed to the corresponding author.

Acknowledgments: To technicians Agustin Vazquez-Escudero and Ivan Castro-Cisneros for their support in the use and handling of characterization equipment. During the preparation of this manuscript/study, the author(s) used: An APD 2000 X-ray diffractometer equipped with Cu Kα radiation (λ = 1.54321 Å), a Cole-Parmer flowmeter (model 32908-59; 1–100 mL/min), and a Hitachi scanning electron microscope operating at an accelerating voltage of 20–30 kV. The authors have reviewed and edited the output and take full responsibility for the content of this publication.

Conflicts of Interest: The authors declare no conflicts of interest.

Abbreviations

The following abbreviations are used in this manuscript:

*SEM**	Standard error of the mean
XRD	X-ray diffraction
SEM	Scanning electron microscopy
NaOH	Sodium hydroxide
$Al(OH)_3$	Aluminum hydroxide
Al_2O_3	Aluminum oxide
$NaAl(OH)_4$	Hydrated sodium aluminate
EDS	Energy-dispersive X-ray spectroscopy
Q_{max}	Maximum flow rate
t_r	Reaction time
SCM	Shrinking core model
F_d	Fractional conversion

References

1. Hassanpouryouzband, A.; Veshareh, M.J.; Wilkinson, M.; Nick, H.M.; Ngwenya, B.T.; Haszeldine, R.S. In Situ Hydrogen Generation from Underground Fossil Hydrocarbons. *Joule* **2025**, *9*, 101809. [CrossRef]
2. Ikpeka, P.M.; Ugwu, J.O. In Situ Hydrogen Production from Hydrocarbon Reservoirs—Modelling Study. *RSC Adv.* **2023**, *13*, 12100–12113. [CrossRef]
3. Seyitoglu, S.S.; Dincer, I.; Kilicarslan, A. Energy and Exergy Analyses of Hydrogen Production by Coal Gasification. *Int. J. Hydrogen Energy* **2017**, *42*, 2592–2600. [CrossRef]
4. Dai, F.; Zhang, S.; Luo, Y.; Wang, K.; Liu, Y.; Ji, X. Recent Progress on Hydrogen-Rich Syngas Production from Coal Gasification. *Processes* **2023**, *11*, 1765. [CrossRef]
5. Muradov, N.; Vezirolu, T. From Hydrocarbon to Hydrogen? Carbon to Hydrogen Economy. *Int. J. Hydrogen Energy* **2005**, *30*, 225–237. [CrossRef]
6. Pant, K.K.; Gupta, R.B. Fundamentals and Use of Hydrogen as a Fuel. In *Hydrogen Fuel: Production, Transport and Storage*; Gupta, R.B., Ed.; CRC Press: Boca Raton, FL, USA, 2008.
7. Gimpel, J.A.; Specht, E.A.; Georgianna, D.R.; Mayfield, S.P. Advances in Microalgae Engineering and Synthetic Biology Applications for Biofuel Production. *Curr. Opin. Chem. Biol.* **2013**, *17*, 489–495. [CrossRef]
8. Moore, R. Economic Feasibility of Advanced Technology for Hydrogen Production from Fossil Fuels. *Int. J. Hydrogen Energy* **1983**, *8*, 905–911. [CrossRef]
9. Boretti, A.; Banik, B.K. Advances in Hydrogen Production from Natural Gas Reforming. *Adv. Energy Sustain. Res.* **2021**, *2*, 2100097. [CrossRef]
10. Halder, P.; Babaie, M.; Salek, F.; Haque, N.; Savage, R.; Stevanovic, S.; Bodisco, T.A.; Zare, A. Advancements in Hydrogen Production, Storage, Distribution and Refuelling for a Sustainable Transport Sector: Hydrogen Fuel Cell Vehicles. *Int. J. Hydrogen Energy* **2024**, *52*, 973–1004. [CrossRef]
11. Nnabuife, S.G.; Ugbeh-Johnson, J.; Okeke, N.E.; Ogbonnaya, C. Present and Projected Developments in Hydrogen Production: A Technological Review. *Carbon Capture Sci. Technol.* **2022**, *3*, 100042. [CrossRef]
12. Tashie-Lewis, B.C.; Nnabuife, S.G. Hydrogen Production, Distribution, Storage and Power Conversion in a Hydrogen Economy—A Technology Review. *Chem. Eng. J. Adv.* **2021**, *8*, 100172. [CrossRef]
13. Bannenberg, L.J.; Heere, M.; Benzidi, H.; Montero, J.; Dematteis, E.M.; Suwarno, S.; Jaroń, T.; Winny, M.; Orłowski, P.A.; Wegner, W.; et al. Metal (Boro-) Hydrides for High Energy Density Storage and Relevant Emerging Technologies. *Int. J. Hydrogen Energy* **2020**, *45*, 33687–33730. [CrossRef]
14. Hammad, A.; Ning, F.; Zou, S.; Liu, Y.; Tian, B.; He, C.; Chai, Z.; Wen, Q.; He, L.; Zhou, X. Aluminum Hydrolysis for Hydrogen Generation Enhanced by Sodium Hydride. *Int. J. Hydrogen Energy* **2024**, *77*, 138–148. [CrossRef]
15. Trowell, K.A.; Goroshin, S.; Frost, D.L.; Bergthorson, J.M. Aluminum and Its Role as a Recyclable, Sustainable Carrier of Renewable Energy. *Appl. Energy* **2020**, *275*, 115112. [CrossRef]
16. Wang, H.-W.; Huang, L.-Y. A Green Energy Closed-Loop System Based on Aluminum. *Energies* **2026**, *19*, 853. [CrossRef]
17. Jayaraman, K.; Chauveau, C.; Gökalp, I. Effects of Aluminum Particle Size, Galinstan Content and Reaction Temperature on Hydrogen Generation Rate Using Activated Aluminum and Water. *Energy Power Eng.* **2015**, *7*, 426–432. [CrossRef]
18. Wang, H.Z.; Leung, D.Y.C.; Leung, M.K.H.; Ni, M. A Review on Hydrogen Production Using Aluminum and Aluminum Alloys. *Renew. Sustain. Energy Rev.* **2009**, *13*, 845–853. [CrossRef]
19. Reda, R.; Ashraf, A.; Magdy, I.; Ragab, M.; Eldabaa, N.; Abo Elmagd, M.; Abdelhafiz, M.; El-Banna, O.; Fouad, A.; Aly, H.A.; et al. An Investigation on the Potential of Utilizing Aluminum Alloys in the Production and Storage of Hydrogen Gas. *Materials* **2024**, *17*, 4032. [CrossRef]
20. Mutlu, R.N.; Kandasamy, J.; Kıymaz, T.B.; Güleryüz, D.; Böncü, E.; Eroğlu, E.; Gökalp, İ. Optimization of Aluminum Hydrolysis Reactions and Reactor Design for Continuous Hydrogen Production Using Aluminum Wire Feeding. *Int. J. Hydrogen Energy* **2024**, *52*, 1390–1403. [CrossRef]
21. Teng, H.-T.; Lee, T.-Y.; Chen, Y.-K.; Wang, H.-W.; Cao, G. Effect of $Al(OH)_3$ on the Hydrogen Generation of Aluminum–Water System. *J. Power Sources* **2012**, *219*, 16–21. [CrossRef]
22. Musicco, N.; Gelfi, M.; Iora, P.; Venturelli, M.; Artioli, N.; Montorsi, L.; Milani, M. A Review of Hydrogen Generation Methods via Aluminum-Water Reactions. *Int. J. Thermofluids* **2025**, *27*, 101152. [CrossRef]
23. Mezulis, A.; Richter, C.; Lesnicenoks, P.; Knoks, A.; Varnagiris, S.; Urbonavicius, M.; Milcius, D.; Kleperis, J. Studies on Water–Aluminum Scrap Reaction Kinetics in Two Steps and the Efficiency of Green Hydrogen Production. *Energies* **2023**, *16*, 5554. [CrossRef]
24. Bolt, A.; Dincer, I.; Agelin-Chaab, M. Experimental Study of Hydrogen Production Process with Aluminum and Water. *Int. J. Hydrogen Energy* **2020**, *45*, 14232–14244. [CrossRef]
25. Dong, Z.; Yao, W.; Niu, F.; Chen, D.; Huang, Y. Hydrogen Generation Dynamics of the Reaction between Metal Aluminum and Sodium Hydroxide Solution under Pressurized Condition. *Int. J. Hydrogen Energy* **2026**, *198*, 152795. [CrossRef]

26. Gorobez, J.; Maack, B.; Nilius, N. Growth of Self-Passivating Oxide Layers on Aluminum—Pressure and Temperature Dependence. *Phys. Status Solidi B* **2021**, *258*, 2000559. [CrossRef]
27. Soler, L.; Macanás, J.; Muñoz, M.; Casado, J. Hydrogen Generation from Aluminum in A Non-Consumable Potassium Hydroxide Solution. In Proceedings of the International Hydrogen Energy Congress and Exhibition IHEC, Istanbul, Turkey, 3–15 July 2005; pp. 1–7.
28. Kaur, P.; Verma, G. A Critical Assessment of Aluminum-Water Reaction for on-Site Hydrogen-Powered Applications. *Mater. Today Energy* **2024**, *40*, 101508. [CrossRef]
29. Martínez-Salazar, A.L.; Melo-Banda, J.A.; Coronel-García, M.A.; González-Barbosa, J.J.; Domínguez-Esquivel, J.M. Hydrogen Generation by Aluminum Alloy Corrosion in Aqueous Acid Solutions Promoted by Nanometal: Kinetics Study. *Renew. Energy* **2020**, *146*, 2517–2523. [CrossRef]
30. Maulana, F.R.; Fadhilah, N.; Wahyuono, R.A.; Risanti, D.D. Hydrogen Production from Waste Aluminum Foil AA1235 Using the Aluminum-Water Reaction Method with Thickness Variations. *Adv. Mat. Res.* **2023**, *1175*, 9–15. [CrossRef]
31. Wanta, K.C.; Astuti, W.; Perdana, I.; Petrus, H.T.B.M. Kinetic Study in Atmospheric Pressure Organic Acid Leaching: Shrinking Core Model versus Lump Model. *Minerals* **2020**, *10*, 613. [CrossRef]
32. Kokoszka, P.; Milenin, A. The Influence of Aging on Buckle Strength Loss in AA5182-H48 for Beverage Can Ends. *Comput. Methods Mater. Sci.* **2023**, *23*, 5–17. [CrossRef]
33. Wang, Z.; Yu, Y.; Jin, Y.; Li, Z.; Sun, S.; Xu, H.; Wu, C.; Zhang, D. Solid State Recycling of Used Aluminum Alloy Beverage Cans by Thermomechanical Consolidation. *Heat Treat. Surf. Eng.* **2022**, *4*, 90–98. [CrossRef]
34. Shi, Y.; Jin, H.; Wu, P.D. Analysis of Cup Earing for AA3104-H19 Aluminum Alloy Sheet. *Eur. J. Mech.—A/Solids* **2018**, *69*, 1–11. [CrossRef]
35. *ASTM E11-22*; Standard Specification for Woven Wire Test Sieve Cloth and Test Sieves. ASTM International: West Conshohocken, PA, USA, 2022. [CrossRef]
36. Soler, L.; Macanás, J.; Muñoz, M.; Casado, J. Aluminum and Aluminum Alloys as Sources of Hydrogen for Fuel Cell Applications. *J. Power Sources* **2007**, *169*, 144–149. [CrossRef]
37. Vogrin, J.; Santini, T.; Peng, H.; Vaughan, J. The Anion Effect on Sodium Aluminosilicates Formed under Bayer Process Digestion Conditions. *Hydrometallurgy* **2020**, *192*, 105236. [CrossRef]
38. Li, H.; Addai-Mensah, J.; Thomas, J.C.; Gerson, A.R. The Crystallization Mechanism of $Al(OH)_3$ from Sodium Aluminate Solutions. *J. Cryst. Growth* **2005**, *279*, 508–520. [CrossRef]
39. Macanás, J.; Soler, L.; Candela, A.M.; Muñoz, M.; Casado, J. Hydrogen Generation by Aluminum Corrosion in Aqueous Alkaline Solutions of Inorganic Promoters: The AlHidrox Process. *Energy* **2011**, *36*, 2493–2501. [CrossRef]
40. Saif, M.T.A.; Zhang, S.; Haque, A.; Hsia, K.J. Effect of Native Al_2O_3 on the Elastic Response of Nanoscale Al Films. *Acta Mater.* **2002**, *50*, 2779–2786. [CrossRef]
41. Belitskus, D. Reaction of Aluminum with Sodium Hydroxide Solution as a Source of Hydrogen. *J. Electrochem. Soc.* **1970**, *117*, 1097. [CrossRef]
42. Wang, X.; Li, G.; Eckhoff, R.K. Kinetics Study of Hydration Reaction between Aluminum Powder and Water Based on an Improved Multi-Stage Shrinking Core Model. *Int. J. Hydrogen Energy* **2021**, *46*, 33635–33655. [CrossRef]
43. Cabrera, N.; Mott, N.F. Theory of the Oxidation of Metals. *Rep. Prog. Phys.* **1949**, *12*, 308. [CrossRef]
44. Qian, X.; Dong, Z.; Jiang, B.; Lei, B.; Yang, H.; He, C.; Liu, L.; Wang, C.; Yuan, M.; Yang, H.; et al. Influence of Alloying Element Segregation at Grain Boundary on the Microstructure and Mechanical Properties of Mg-Zn Alloy. *Mater. Des.* **2022**, *224*, 111322. [CrossRef]
45. Abdelghani-Idrissi, S.; Dubouis, N.; Grimaud, A.; Stevens, P.; Toussaint, G.; Colin, A. Effect of Electrolyte Flow on a Gas Evolution Electrode. *Sci. Rep.* **2021**, *11*, 4677. [CrossRef] [PubMed]
46. Urbonavicius, M.; Varnagiris, S.; Girdzevicius, D.; Milcius, D. Hydrogen Generation Based on Aluminum-Water Reaction for Fuel Cell Applications. *Energy Procedia* **2017**, *128*, 114–120. [CrossRef]
47. Gai, W.-Z.; Wang, L.-Y.; Lu, M.-Y.; Deng, Z.-Y. Effect of Low Concentration Hydroxides on Al Hydrolysis for Hydrogen Production. *Energy* **2023**, *268*, 126731. [CrossRef]
48. Deng, Z.; Zhu, L.; Tang, Y.; Sakka, Y.; Ye, J.; Xie, R. Role of Particle Sizes in Hydrogen Generation by the Reaction of Al with Water. *J. Am. Ceram. Soc.* **2010**, *93*, 2998–3001. [CrossRef]
49. González-Solórzano, M.G.; Morales, R.; Ávila, J.R.; Muñiz-Valdés, C.R.; Bastida, A.N. Alumina Nucleation, Growth Kinetics, and Morphology: A Review. *Steel Res. Int.* **2023**, *94*, 2200678. [CrossRef]
50. Aleksandrov, Y.A.; Tsyganova, E.I.; Pisarev, A.L. Reaction of Aluminum with Dilute Aqueous NaOH Solutions. *Russ. J. Gen. Chem.* **2003**, *73*, 689–694. [CrossRef]
51. Poznyak, A.; Pligovka, A.; Turavets, U.; Norek, M. On-Aluminum and Barrier Anodic Oxide: Meeting the Challenges of Chemical Dissolution Rate in Various Acids and Solutions. *Coatings* **2020**, *10*, 875. [CrossRef]

52. Bolt, A.; Dincer, I.; Agelin-Chaab, M. A Review of Unique Aluminum–Water Based Hydrogen Production Options. *Energy Fuels* **2021**, *35*, 1024–1040. [CrossRef]
53. Cuzacq, L.; Silvain, J.-F.; Sabatier, J.; Bobet, J.-L. Hydrogen Production by Hydrolysis of Bulk Porous Aluminum. *ACS Appl. Energy Mater.* **2025**, *8*, 7394–7401. [CrossRef]
54. Abdelkareem, M.A.; Ayoub, M.; Al Najada, R.I.; Alami, A.H.; Olabi, A.G. Hydrogen from Waste Metals: Recent Progress, Production Techniques, Purification, Challenges, and Applications. *Sustain. Horiz.* **2024**, *9*, 100079. [CrossRef]
55. Salueña-Berna, X.; Marín-Genescà, M.; Mujal Rosas, R.; Arias, M.-J.L. Controlled and Safe Hydrogen Generation from Waste Aluminum and Water, a New Approach to Hydrogen Generation. *Materials* **2024**, *17*, 5885. [CrossRef]
56. Shmelev, V.; Nikolaev, V.; Lee, J.H.; Yim, C. Hydrogen Production by Reaction of Aluminum with Water. *Int. J. Hydrogen Energy* **2016**, *41*, 16664–16673. [CrossRef]
57. Trowell, K.; Goroshin, S.; Frost, D.; Bergthorson, J. Hydrogen Production Rates of Aluminum Reacting with Varying Densities of Supercritical Water. *RSC Adv.* **2022**, *12*, 12335–12343. [CrossRef]
58. Gao, Z.; Ji, F.; Cheng, D.; Yin, C.; Niu, J.; Brnic, J. Hydrolysis-Based Hydrogen Generation Investigation of Aluminum System Adding Low-Melting Metals. *Energies* **2021**, *14*, 1433. [CrossRef]
59. Razavi-Tousi, S.S.; Szpunar, J.A. Modification of the Shrinking Core Model for Hydrogen Generation by Reaction of Aluminum Particles with Water. *Int. J. Hydrogen Energy* **2016**, *41*, 87–93. [CrossRef]

Disclaimer/Publisher's Note: The statements, opinions and data contained in all publications are solely those of the individual author(s) and contributor(s) and not of MDPI and/or the editor(s). MDPI and/or the editor(s) disclaim responsibility for any injury to people or property resulting from any ideas, methods, instructions or products referred to in the content.